

Structure-property relationships of an A36 steel alloy under dynamic loading conditions

By

Adam J. Mayatt

A Thesis
Submitted to the Faculty of
Mississippi State University
in Partial Fulfillment of the Requirements
for the Degree of Master of Science
in Mechanical Engineering
in the Department of Mechanical Engineering

Mississippi State, Mississippi

December 2012

UMI Number: 1530746

All rights reserved

INFORMATION TO ALL USERS

The quality of this reproduction is dependent upon the quality of the copy submitted.

In the unlikely event that the author did not send a complete manuscript and there are missing pages, these will be noted. Also, if material had to be removed, a note will indicate the deletion.



UMI 1530746

Published by ProQuest LLC (2012). Copyright in the Dissertation held by the Author.

Microform Edition © ProQuest LLC.

All rights reserved. This work is protected against unauthorized copying under Title 17, United States Code



ProQuest LLC.
789 East Eisenhower Parkway
P.O. Box 1346
Ann Arbor, MI 48106 - 1346

Copyright by
Adam J. Mayatt
2012

Structure-property relationships of an A36 steel alloy under dynamic loading conditions

By

Adam J. Mayatt

Approved:

Mark F. Horstemeyer
Professor of Mechanical Engineering
(Director of Thesis)

Bin Li
Assistant Research Professor
of Mechanical Engineering
(Committee Member)

Hongjoo Rhee
Assistant Research Professor
of Mechanical Engineering
(Committee Member)

Steven R. Daniewicz
Professor and Head of Mechanical
Engineering
(Graduate Coordinator)

Sarah A. Rajala
Dean of the Bagley College of Engineering

Name: Adam J. Mayatt

Date of Degree: December 15, 2012

Institution: Mississippi State University

Major Field: Mechanical Engineering

Major Professor: Mark Horstemeyer

Title of Study: Structure-property relationships of an A36 steel alloy under dynamic loading conditions

Pages in Study: 37

Candidate for Degree of Master of Science

Structure-property quantification of an A36 steel alloy was the focus of this study in order to calibrate and validate a plasticity-damage model. The microstructural parameters included grain size, particle size, particle number density, particle nearest neighbor distances, and percent of ferrite and pearlite. The mechanical property data focused on stress-strain behavior under different applied strain rates (0.001/s, 0.1/s, and 1000/s), different temperatures (293 K and 573 K), and different stress states (compression, tension, and torsion). Notch tension tests were also conducted to validate the plasticity-damage model. Also, failure of an A36 I-beam was examined in cyclic loads, and the crack growth rates were quantified in terms of fatigue striation data. Dynamic strain aging was observed in the stress-strain behavior giving rise to an important point that there exists a critical temperature for such behavior.

TABLE OF CONTENTS

LIST OF TABLES	iii
LIST OF FIGURES	iv
CHAPTER	
I. INTRODUCTION	1
II. MATERIAL AND EXPERIMENTAL PROCEDURES.....	4
III. RESULTS AND DISCUSSION.....	10
IV. A36 STEEL ALLOY I-BEAM.....	25
V. CONCLUSION.....	30
REFERENCES	31
APPENDIX	
A. MICROSTRUCTURE-PROPERTY MODEL EQUATIONS (MACROSCALE).....	32
B. MECHANICAL SPECIMENS.....	35

LIST OF TABLES

2.1	ASTM A36/A 36M Chemical Composition by Weight %	4
2.2	A36 steel as received Chemical Composition by Weight %.....	4
3.2	Characteristics of A36 steel.....	22
3.3	The number density of voids observed on the fracture specimens.....	24
4.1	I-Beam composition chemical composition by weight %.....	25

LIST OF FIGURES

2.1	Iron / carbon phase diagram. Note that the A36 steel alloy has 0.25% max carbon content.	5
2.2	Tension stress-strain behavior for A36 alloy plate showing the isotropic behavior from the longitudinal (rolling direction) and transverse directions. If anisotropy from texture were present, the stress-strain behavior would be different.	6
2.3	Mechanical testing Matrix.....	7
3.1	Dynamic strain aging captured during tensile test are illustrated by the intermittent bumps in the stress-strain curve and the local shear bands in the microstructural analysis. The Luders band picture is from Wang et al., [2012].	11
3.2	Experimental data from Murty et.al. [1998] and that generated from the current study.....	13
3.3	Experimental compression stress-strain behavior of A36 steel under varying strain rates at 293K.	14
3.4	Experimental compression stress-strain behavior of A36 steel under quasi-static loading at two different temperatures.	15
3.5	Tensile stress-strain behavior of an A36 steel alloy plate under different applied strain rates at 293K and also showing the effect of different specimen size.....	16
3.6	Stress-strain behavior of an A36 steel alloy under compression at a temperature of 573K.....	17
3.7	Experimental tensile stress-strain behavior of A36 steel plate under varying strain rates at two different temperatures with error bars. The trend that as the work hardening rate is greater for the higher temperature illustrates the effect of dynamic strain aging.	18
3.8	Torsional stress-strain behavior of an A36 steel alloy at 293K.	19

3.9	Comparison of the plasticity-damage internal state variable model with the experimental stress-strain behavior for A36 steel alloy under varying strain rates at 293K.	20
3.10	Hot mount of as-received A36 steel alloy sample showing face (A), side (B), and edge (C).	21
3.11	Grains structure of A36 steel alloy from optical microscope; the light area is ferrite and dark areas are pearlite.	22
3.12	Tensile fracture surface from an applied strain rate of 0.001/s at 273 K.	23
3.13	Tensile fracture surface at a strain rate of 0.1/s at 273 K.	23
3.14	Tensile fracture surface at a strain rate of 1000/s at 273 K.	23
3.15	Load-displacement curve of notch A36 steel alloy specimens at two different applied strain rates (0.001/s and 0.1/s).	24
4.1	Cracks from A36 steel I-beams.	26
4.2	Instron 8850 and I-beam section.	26
4.3	Final reduced crack section used for analysis, and the image of beachmarks and striations.	27
4.4	Striation measurements and crack growth rate.	28
4.5	Ambient compression test comparing A36 plate steel and I-beam.	29
A.1	Constants for MSU Internal State Variable Plasticity-Damage Model.	34
B.1	Mechanical test notch specimen.	36
B.2	Mechanical test specimens.	37

CHAPTER I

INTRODUCTION

This experimental research quantifies the structure-property relationships to calibrate and validate the Mississippi State University (MSU) plasticity-damage model for A36 plate steel alloy. Literature is sparse for A36 steel, although this particular steel alloy has been in ubiquitous use as a structural member. According to the Metals Handbook (ASM International, Metals Handbook), A36 is the most common structural steel used in construction, because of its strength and weldability. While the diffusion of the A36 steel alloy into industry occurred on a large scale, the mechanical properties and the microstructural characterization were investigated just enough to put it into use. In this research the results of varying strain rates, temperatures, and stress states provides further insight into the applications of A36 steel for use in failure analysis. The failure mechanisms of the A36 steel alloys were characterized under monotonic (fracture) and cyclic environments (fatigue).

The mechanical testing comprised compression, tension, and torsion at ambient temperature (293K) at three different strain rates (0.001/s, 0.1/s and 1000/s). Mechanical testing was also performed at 573 degrees Kelvin (K) for compression and tension at strain rates of 0.001/s and 0.1/s. A high temperature capability for high rates is not yet available nor is it available for torsion at the MSU/CAVS facility. Metallurgical analysis

provided grain size, particle size, and volume fraction information in order to find model constants for calibration and validation the plasticity model.

In Murty's et. al [1998] article testing was nondestructive in nature using an automated ball indentation technique (ABI). Murty's application was in the nuclear industry in order to determine toughness degradation due to aging in service (Murty et al. [1998]) so late rate phenomena was observed but no stress state temperature was analyzed. Other research to determine fracture behavior of A36 pertaining to bridge steel was conducted at varying temperatures using the Charpy V-notch tests (Roberts, Krishna, and Nishanian), but the microstructural details were not quantified. High rate impact scenarios for Explosive Ordnance Disposal (EOD) using controlled ballistic impact testing research was conducted by Seidt et al., [2007], who studied A36 under high rates in order to accurately predict the impact of a projectile fired on ordinance in order to make the disposal process more efficient. Although high rate torsion and tensile Hopkinson bar [1914] testing were conducted by Seidt et al. [2007] to determine model constants for the Johnson-Cook [1983] plasticity-failure model, they did not characterize the material microstructure because the Johnson-Cook Model does not admit it.

The objective of this research is to quantify the failure mechanisms of A36 steel undergoing plasticity at varying strain rates, temperatures, and stress states with a goal to use an internal state variable plasticity-model that admits microstructural details like that of Bammann et al. [1993] and Horstemeyer et al., [2000]. The model (shown in the appendix) constants are then determined from the experimental data. The monotonic experiments (compression, tension, and torsion) are used from the model calibration, and experiments with notch specimens are used to validate the model. Another experiment

was conducted in which an A36 steel I-beam from industry was examined after failure in use. Although the full gamut of modeling was not conducted in this research, the results provide the fodder for a full to be accomplished. The contribution is the quantification of the damage/failure under the different scenarios since the A36 steel has been widely used over the past 100 years in structures such as bridges, buildings, and military bulwarks.

Different genre of A36 plate steel alloy was compared from different sources; military rolled plate material and a hoist support I-Beam from a local manufacturing company. The I-Beam was in use for several years and developed low cycle fatigue cracks in several places on the ninety-four foot I-Beam. The cracking was thought to have been caused by on overloading of the beam capacity at 16000 pounds where the beam was only rated for an 8000 pound capacity by the lead engineer. The crack locations found on the I-beam were isolated and reduced to manageable pieces in order to perform analysis on the cracks. The smaller sections of I-Beam were pulled apart by an Instron 8850 hydraulic load frame in order to investigate the fractured surface where the cracks developed. Mechanical testing was conducted from a sample piece of the I-beam for compression at rates of 0.001/s and 0.1/s strain rates. The test data was then compared to the A36 plate steel alloy.

CHAPTER II
MATERIAL AND EXPERIMENTAL PROCEDURES

Hot rolled plate of A36 steel alloy, 1.5 inches thick, is the material mainly used in this study. According to the ASTM standard for 0.75 to 1.5 inch plate the chemical by weight percentage requirements for A36 steel are shown in Table 2.1 (ASM Handbook, 2002). The actual as-received plate steel chemical composition by weight percentage in Table 2.2 was determined by using a Spectrometer analysis. The ASTM standard for A36 steel alloy labels this steel as a low carbon structural steel. Tensile yield for A36 is 36,300 psi. The nomenclature A36 can also be expressed as A36/A where the A designates this steel meets ASTM standards.

Table 2.1 ASTM A36/A 36M Chemical Composition by Weight %

Element Wt. %					ASTM
C	Mn	P	S	Si	Cu
0.250 max	0.80 – 1.20	0.040 max	0.05 max	0.40 max	0.20 min

Table 2.2 A36 steel as received Chemical Composition by Weight %

Element Wt. %					As received
C	Mn	P	S	Si	Cu
0.208	1.12	0.005	0.02	0.28	0.25

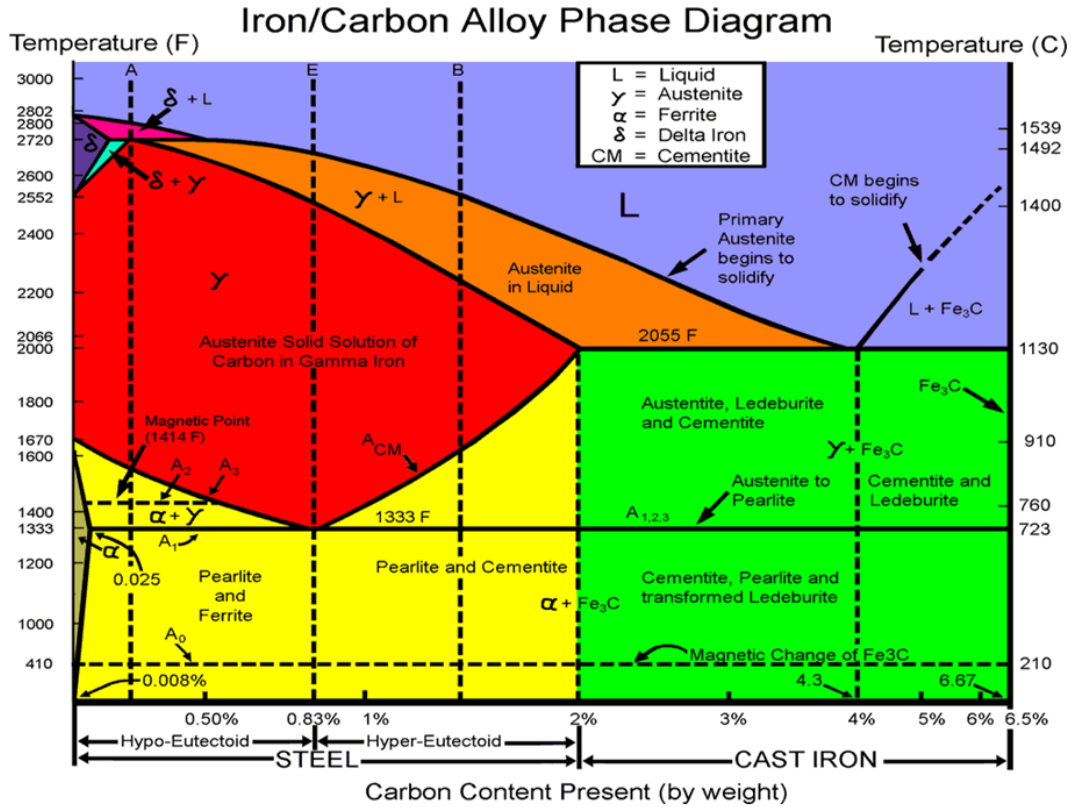


Figure 2.1 Iron / carbon phase diagram. Note that the A36 steel alloy has 0.25% max carbon content.

The alloying elements contribute to different properties to steel alloys, essentially, Manganese improves the strength and workability of steel at high temperatures; Copper contributes to strength also but more importantly to the corrosion resistance. Sulfur allows for better machinability, and finally Silicon facilitates deoxidization and hardness [ASM Handbook, 2002]. Also noted here is that the A36 steel alloy is a low cost steel.

Among the many mechanical properties discussed in this paper, we quantified that the A36 plate material was isotropic. Figure 2.2 shows the stress-strain behavior of the A36 steel alloy in tension, showing the longitudinal and transverse directions.

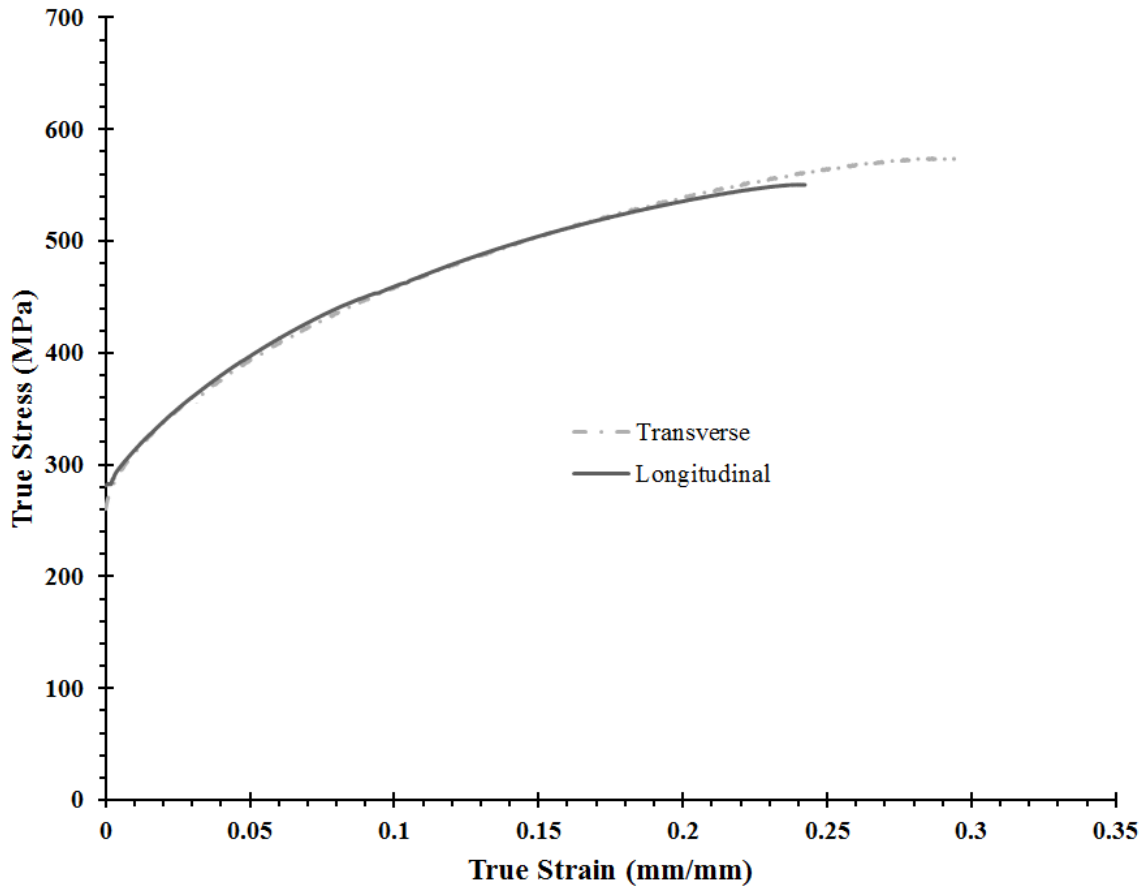


Figure 2.2 Tension stress-strain behavior for A36 alloy plate showing the isotropic behavior from the longitudinal (rolling direction) and transverse directions. If anisotropy from texture were present, the stress-strain behavior would be different.

Once no directional dependence was determined the specimens were machined according to the test specimen definitions for compression, tension, and torsion shown in Appendix B. Figure 3.2 shows the test matrix. Compression and tension testing was also performed at an elevated temperature of 573 K but only for the quasi-static tests. As mentioned earlier, temperature chambers were not available for Hopkinson bar testing in tension, compression, or torsion. The quasi – static torsion tests are performed on an

MTS 858 load frame. Notch specimen tests in tension were performed for the final validation of plasticity-damage model constants.

A36 steel				Tests
Loading	Temp (C)	Strain rate	Samples	Machine
Compression	ambient	0.1/s	2	Instron 5882
	ambient	0.001/s	2	Instron 5882
	ambient	High rate- Hopkinson bar	2	Hopkinson
	300	0.1/s	2	Instron 5882
	300	0.001/s	2	Instron 5882
	Tension	ambient	0.1/s	2
	ambient	0.001/s	2	Instron 5882
	ambient	High Rate-Hopkinson Bar	2	Hopkinson
	300	0.1/s	2	Instron 5882
	300	0.001/s	2	Instron 5882
Shear/Torsion	ambient	0.1/s effective	2	MTS 858
	ambient	0.001/s effective	2	MTS 858
	ambient	High Rate-Hopkinson Bar	2	Hopkinson
Notch Tensile	ambient	0.1/s	1	Instron 5882
	ambient	0.001/s	1	Instron 5882

Figure 2.3 Mechanical testing Matrix

Mechanical testing was performed on an Instron 5882 load frame for all quasi-static compression and tension tests at ambient temperature and at the elevated temperature of 573 K. An environmental chamber was used with the Instron load frame for elevated temperature testing. High rate, dynamic loading, tests are performed with Hopkinson bars for compression, tension, and torsion. Load frame calibration was verified, and all extensometers were calibrated before testing was performed. Prior to testing the gage section width, thickness, and length were recorded. With the specimens mounted in the gripping devices, a visual check is made to verify that the centerline of

the specimen was centered with the centerline of the grips to ensure no binding moments or shearing loads were introduced. The tests were terminated manually after breakage of the specimen as evidenced by a load drop. A laser extensometer was utilized for the compression specimens and the tensile specimens with the 0.25 inch gage length. The 2 inch gage length tensile specimens were controlled by an extensometer during testing. Torsion data was recorded from the MTS 858 software and the load cell controlled the test and measured the extension. All specimen dimensions and tolerances are recorded in Figure B1.

Cylindrical compression specimens were machined and used for both Hopkinson bar tests and quasi-static tests. Two different gage lengths of flat coupons were used for quasi-static tensile tests and a much smaller flat specimen was used for the high rate tests. For torsion specimens the Lindholm type was used.

The high strain rate compression tests were conducted using a split Hopkinson pressure bar (Kolsky [1949]) apparatus with striker, incident, and transmitted bars. The cylindrical compression specimen was loaded by a stress wave propagated by the striker bar impacting the incident bar when compressed air from a cylinder is released. As the wave moves through the specimen, a portion of the wave is reflected back through the incident bar, and the remainder of the wave is passed through to the transmitted bar. The incident and reflected bars remain elastic during the testing and act as force and displacement transducers during the test. Using the DAVID software package Gary (2005) the high strain rate compression data was analyzed. DAVID software compensates for the inherent dispersion of the wave and the calculation of the force and velocities at both faces of the specimen during the test to verify force equilibrium.

High strain rate tensile and torsion tests are performed on similar load frames, which use stored loading mechanisms including a rapid release clamp, cable, and pulley system. Before a specimen is set for the tension test a clamp restricts movement of the charged bar. The tensile specimen is placed in between two clamps that are machined to hold this specific specimen for which no epoxy is needed. However the torsional high strain rate bar requires that the specimen be fixed in between two separate bars with a high grade epoxy then given ample time to cure. Once the torsion specimen is ready the rapid release clamp is applied to the section of the bar that will have a stored torque applied. In both test the tensile and torsion the test is initiated as soon as the rapid release clamps are disengaged.

CHAPTER III

RESULTS AND DISCUSSION

Dynamic strain aging is commonly associated with yield point phenomenon and common in low carbon steels, such as A36 structural steel [Dieter, 1986]. The serrations shown in Figure 3.1 are a result of dynamic strain aging and occurred during low strain rate testing at an elevated temperature of 573K.

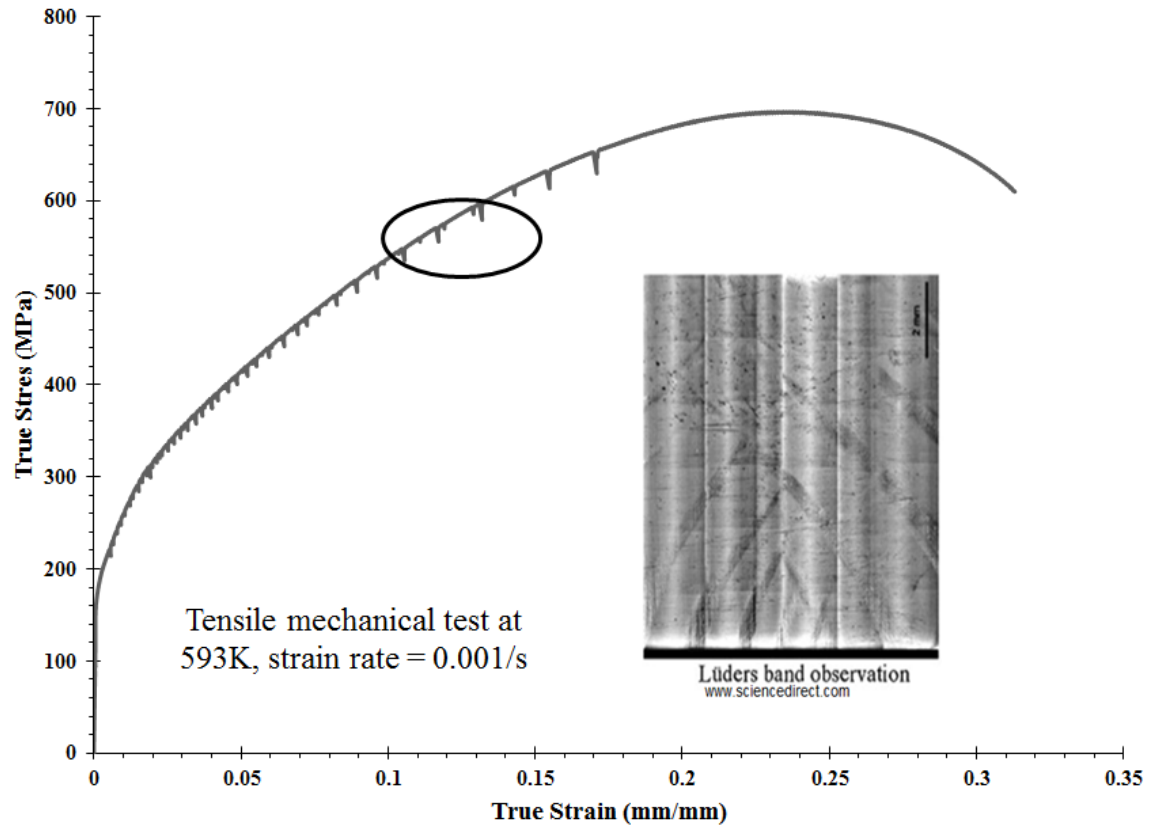


Figure 3.1 Dynamic strain aging captured during tensile test are illustrated by the intermittent bumps in the stress-strain curve and the local shear bands in the microstructural analysis. The Luders band picture is from Wang et al., [2012].

A material experiencing strain aging has an increase in strength and as a consequence a decrease in ductility when experiencing elevated temperatures opposite of what is typical for a ductile metal. As strain aging produces a lower ductility, a low strain rate sensitivity is also observed. The discontinuous or repeated yielding represented by the serrations in the stress-strain behavior is called the Portevin-LeChatelier effect. These serrations are a depiction of a process that repeatedly occurs. Solute atoms can diffuse at a greater rate than dislocations can move thus causing a pile-up of dislocations to stop dislocation movement. An increase of load then builds that eventually moves the

dislocations though the solute atoms thus causing a load drop. Mechanical twinning that occurs during deformation and stress assisted martensitic transformations can also potentially produce the serrations in a stress strain curve [Dieter, 1986].

Similar to the Portevin-LeChatelier effect is that of Luders bands. Found originally in low carbon steel, Luders bands occur during yield-point elongation after the initial yield, also called the upper yield, where the load drops to a lower yield point. Bands form along this yield elongation at points of stress concentration. Luders bands usually are oriented at a 45 degree angle to the tensile axis. After the Luders bands propagate through the gage length of the specimen the test flow will increase with strain and follow their usual behavior.

For low carbon steels, dynamic strain aging occurs between 505K and 645K. This interval of temperatures is also known as the blue brittle region. When embrittlement occurs at elevated temperatures test specimens turn a bright blue color caused by oxides. Blue brittleness is not a separate phenomenon but accelerated strain aging [Dieter, 1986]. Plastic deformation occurs with dynamic strain aging, which is not necessary for age hardening to occur. Figure 3.2 shows the temperature dependence on the ultimate stress, and the start of the dynamic strain aging process is represented by the vertical line with the arrow pointing to the right. The trend of the parabolic line is consistent with embrittlement taking place as the temperature increases and subsequently the UTS increases. Simultaneously, but not shown, the ductility decreases when the UTS increases and the ductility increases when the UTS decreases.

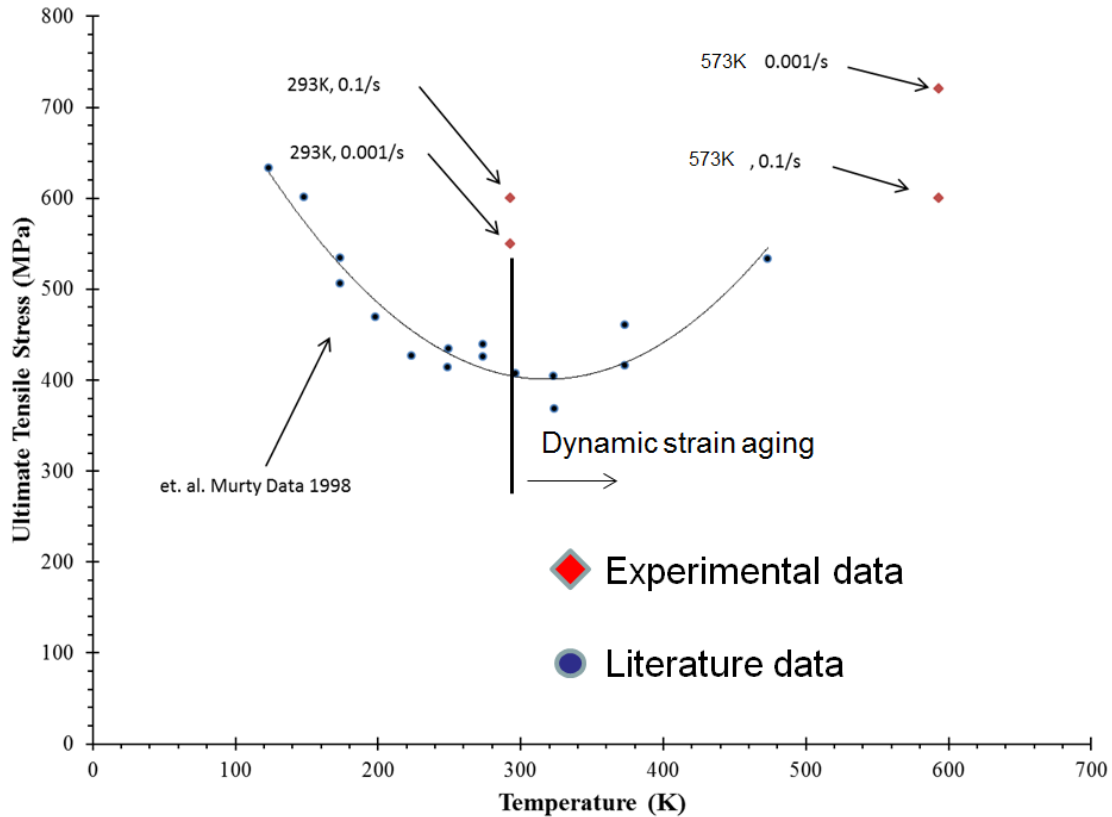


Figure 3.2 Experimental data from Murty et.al. [1998] and that generated from the current study.

Since dynamic strain aging is a common occurrence in low carbon steels, this behavior cannot be neglected in the plasticity model. In order to predict the behavior of strain aging in a model the constants of the stress strain behavior must first be quantified. The experimental data that follows are the results of mechanical testing performed in compression, tension, and torsion. The first series of tests shown in Figure 3.3 represents the stress – strain behavior of compression tests completed at 293K.

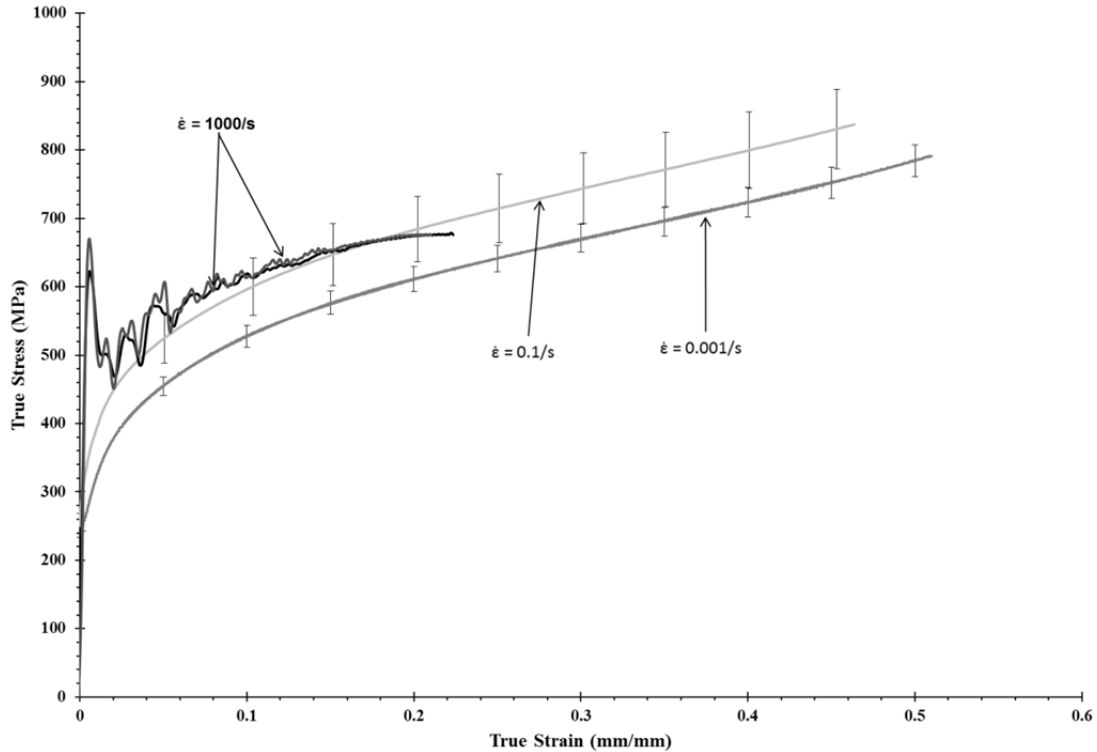


Figure 3.3 Experimental compression stress-strain behavior of A36 steel under varying strain rates at 293K.

Note the increase of yield stress as the applied strain rate increases.

The quasi-static ambient temperature tests performed at strain rates of 0.001/s and 0.1/s have a yield of 260 to 320 MPa, respectively. These yield values are slightly greater than the reported yield by Murty et al. [1998]. One difference may be due to the grain size, which was not determined in the Murty et al. data [1998]. Another difference may be due to the specimen size as will be discussed later. Error bars are included with the stress- strain curves illustrating the repeatability of the tests. The high strain rate tests gave a yield stress at 650MPa, which is much greater than the quasi-static test results. An

average strain rate of 1000/s was calculated using a stress versus time plot, and this high strain rate remained consistent throughout the tension and torsion high strain rate tests.

Figure 3.4 represents the experimental data for quasi-static compression test at 283K and 573K with error bars illustrating the dynamic strain aging effect; that is, as the strain rate increased, the stress state decreased at the higher temperature beyond the strain aging critical temperature. The stress- strain behavior due to dynamic strain aging is consistent throughout the tensile and torsion test data as well. All of the stress-strain curves do not show the serrations, because they were averaged to give the mean values.

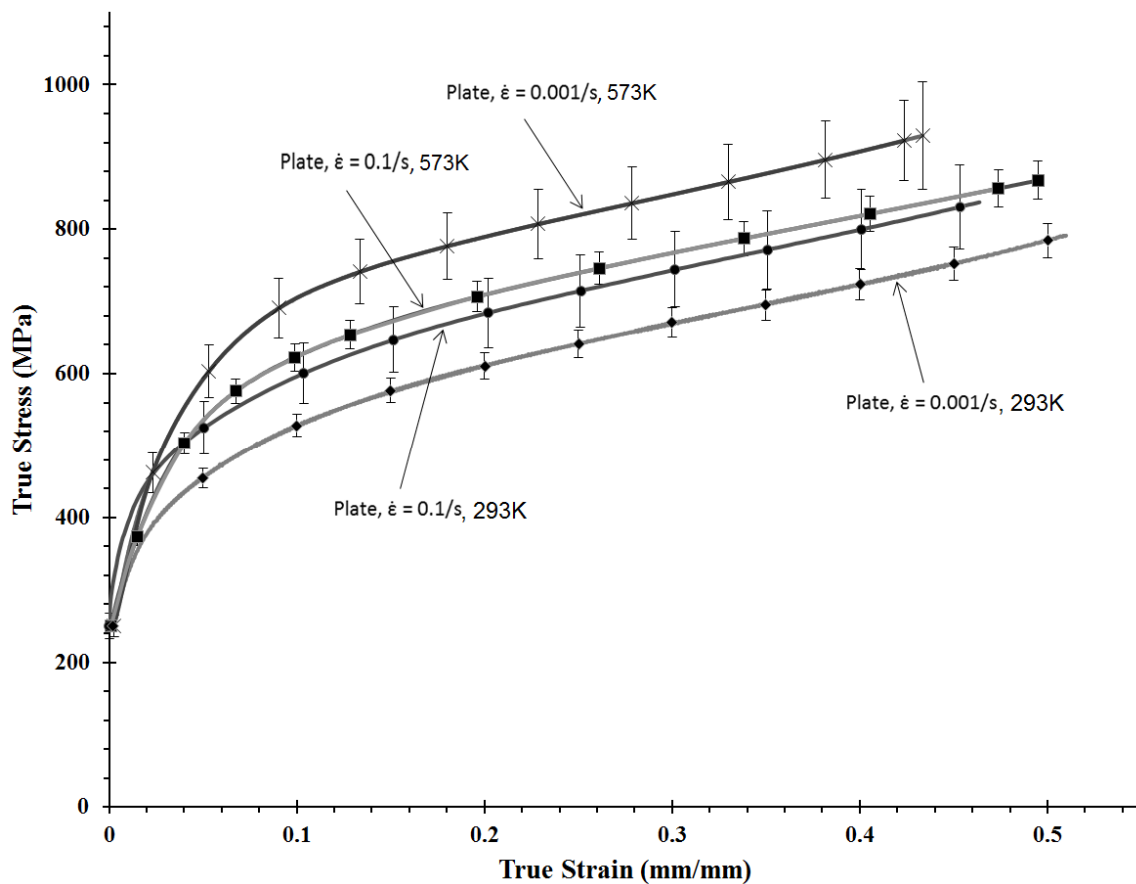


Figure 3.4 Experimental compression stress-strain behavior of A36 steel under quasi-static loading at two different temperatures.

Figure 3.5 shows the experimental stress-strain behavior of the A36 steel alloy under tension. The quasi-static strain rates show a yield strength that increases from 260MPa to 320 MPa associated with applied strain rates of 0.001/s to 0.1/s, respectively, which is consistent with the compression data. However the ultimate tensile strength is lower than for the compression tests at the same rates for both quasi static and high strain rates due to the damage progression till failure.

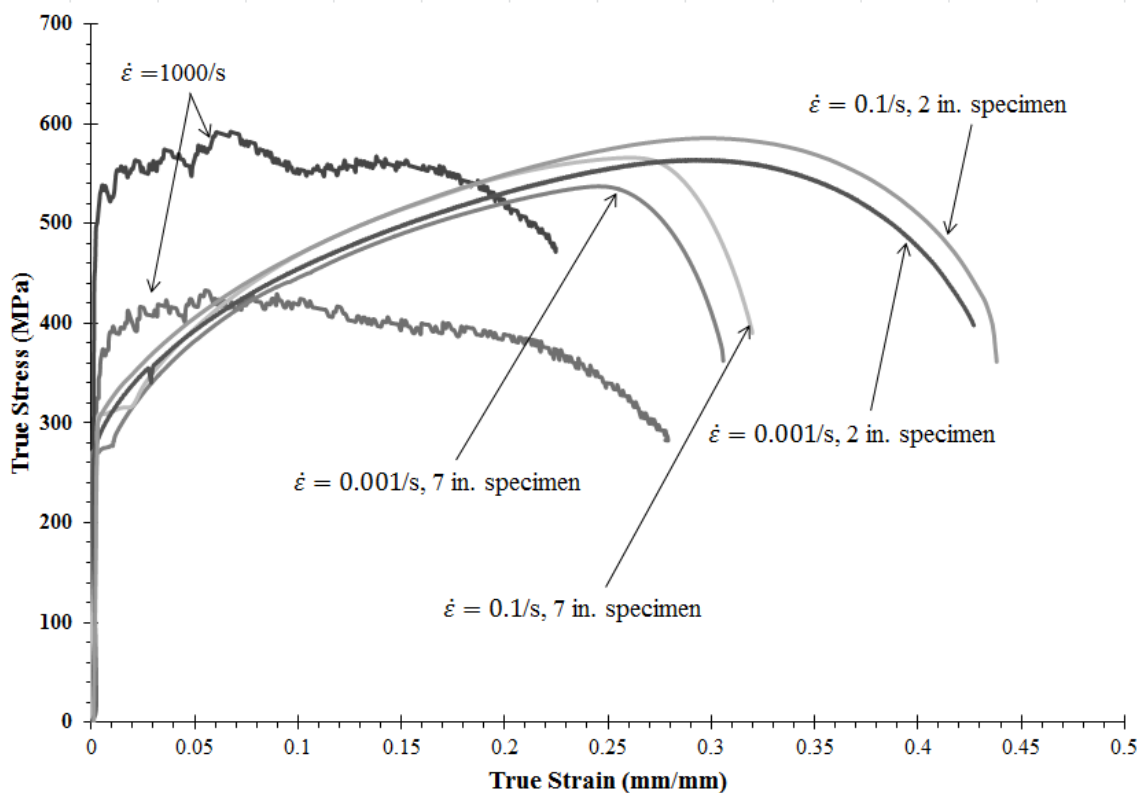


Figure 3.5 Tensile stress-strain behavior of an A36 steel alloy plate under different applied strain rates at 293K and also showing the effect of different specimen size.

The sensitivity between the two different gage lengths to the ductility was remarkable, although both specimens showed a discernible upper and lower yield points

as well as similar hardening rates. Figure 3.6 represents the data for the elevated temperature test performed at 0.001/s and 0.1/s strain rates. As mentioned previously the dynamic strain aging effects are easier to realize in the tension specimens than in the compression. The blue brittle region is also validated by the fact that all of the tensile specimens were a bright blue after completing the tension tests at the elevated temperature of 573K.

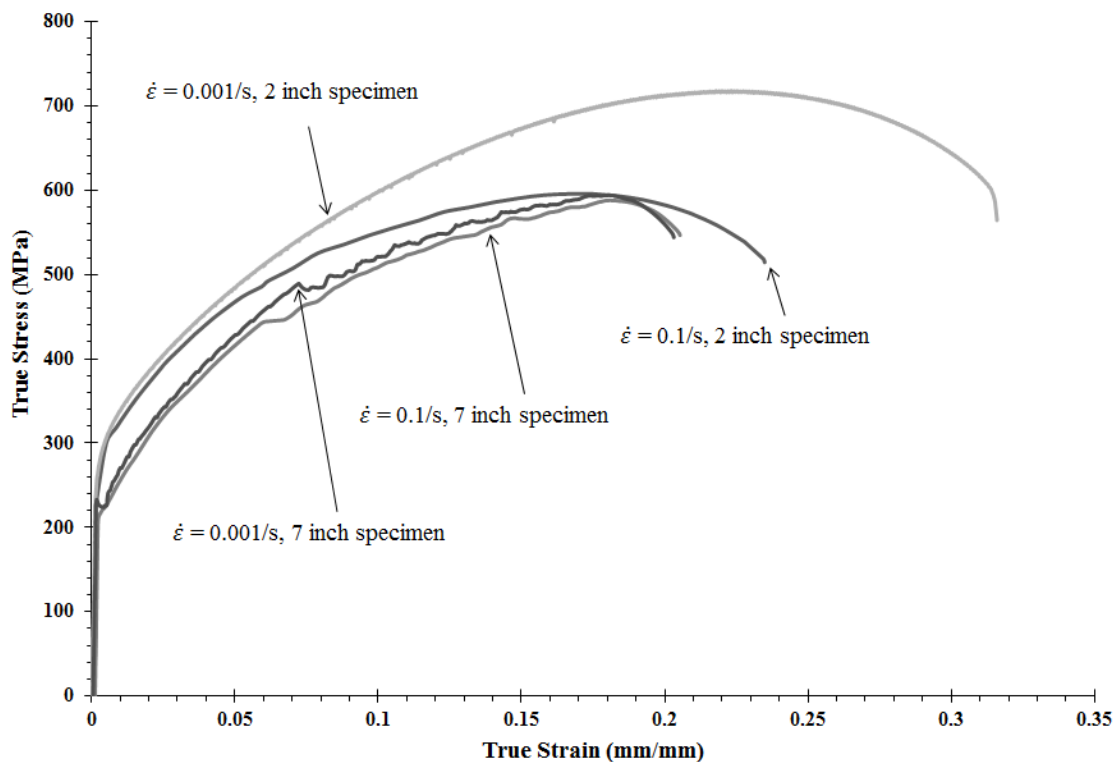


Figure 3.6 Stress-strain behavior of an A36 steel alloy under compression at a temperature of 573K.

The remaining comparison of the ambient and elevated temperature tests in tension are represented in Figure 3.7. Here the smooth curves represent the same tension curves as the serrated curves shown in previous figures. The trend continues, as the data

shows, the opposite behavior in the ambient and elevated temperatures for the lower strain rates. Stress increases as temperature increase at the higher temperature of 573K.

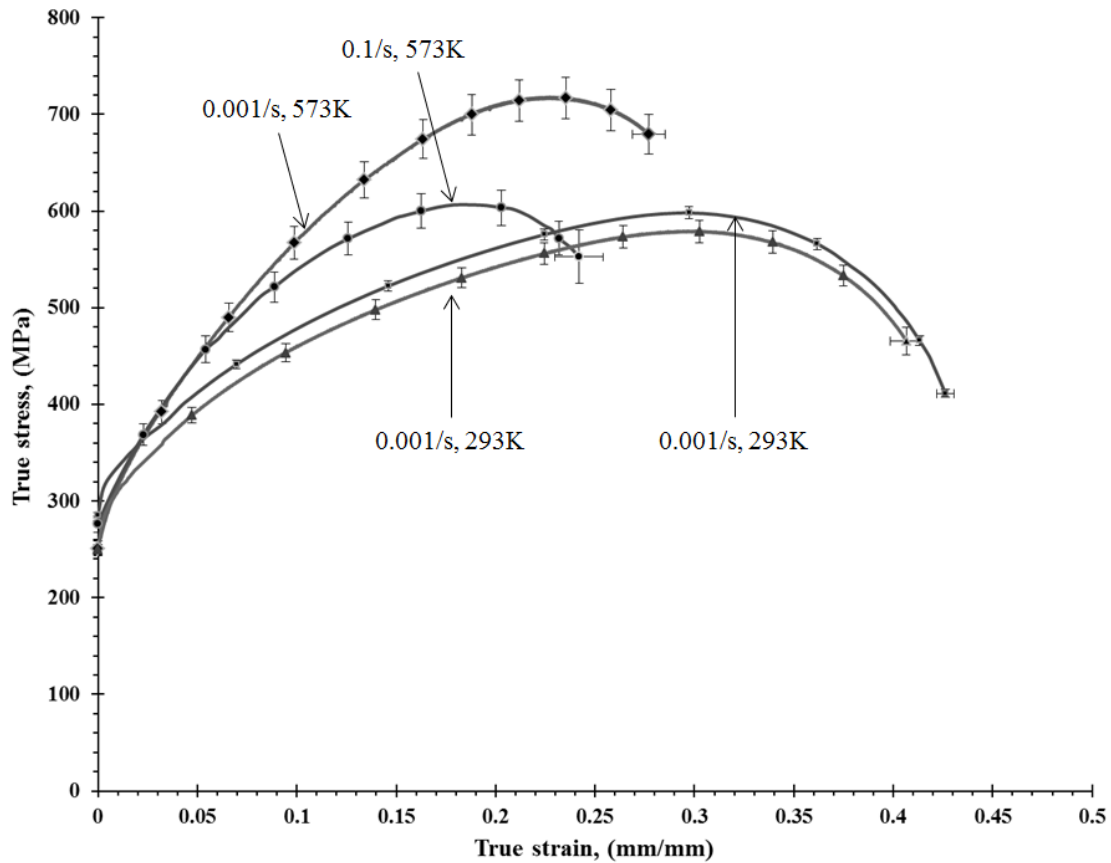


Figure 3.7 Experimental tensile stress-strain behavior of A36 steel plate under varying strain rates at two different temperatures with error bars. The trend that as the work hardening rate is greater for the higher temperature illustrates the effect of dynamic strain aging.

The last series of tests performed consist of torsion at high strain rate and quasi-static strain rates of 0.001/s and 0.1/s at ambient temperature (293 K). Quasi-static yield for torsion was 260MPa to up to 350MPa. There seems to be more variation with the 0.1/s strain rate possibly due to compliance of the load frame. As with the compression

and tension high strain rate tests the upper and lower yield show up very well in the data at approximately 600MPa.

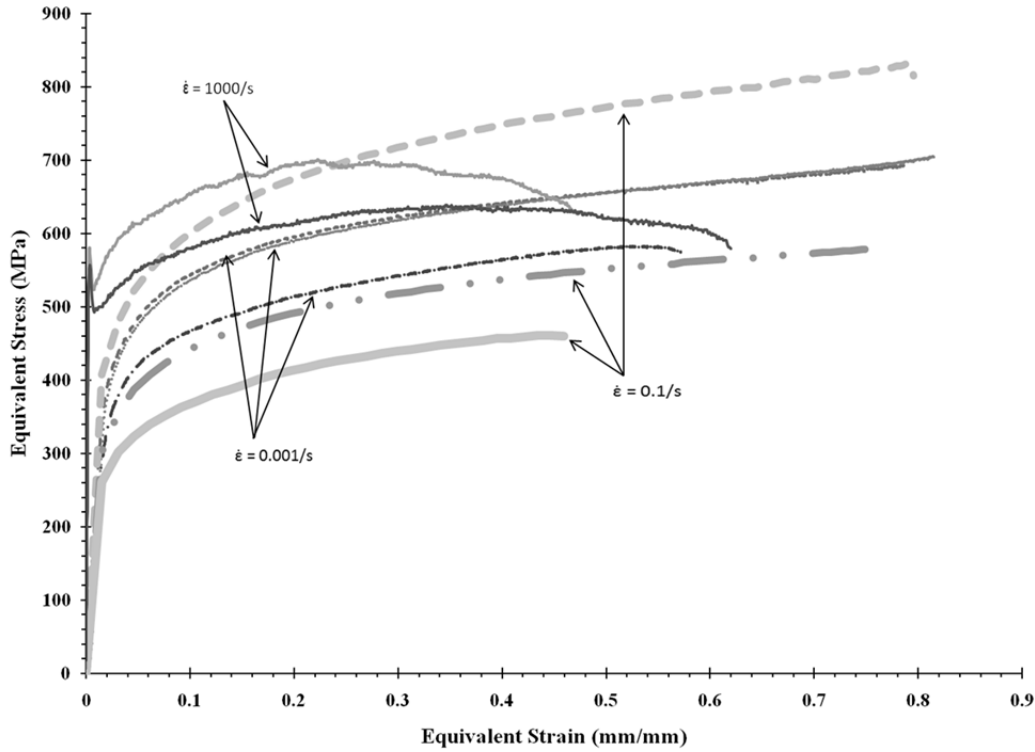


Figure 3.8 Torsional stress-strain behavior of an A36 steel alloy at 293K.

Once the data was collected the MSU plasticity-damage model constants were and the results are shown in Figure 3.9. Here, the dynamic strain aging is not included nor the torsional data. Modifications to the MSU plasticity-damage model to include the dynamic strain aging will occur in the future. The solid curves in the Figure 3.9 represent the model of the experimental data represented by the broken lines. Constants for the stress-strain behavior at ambient temperature are listed in Figure A.1.

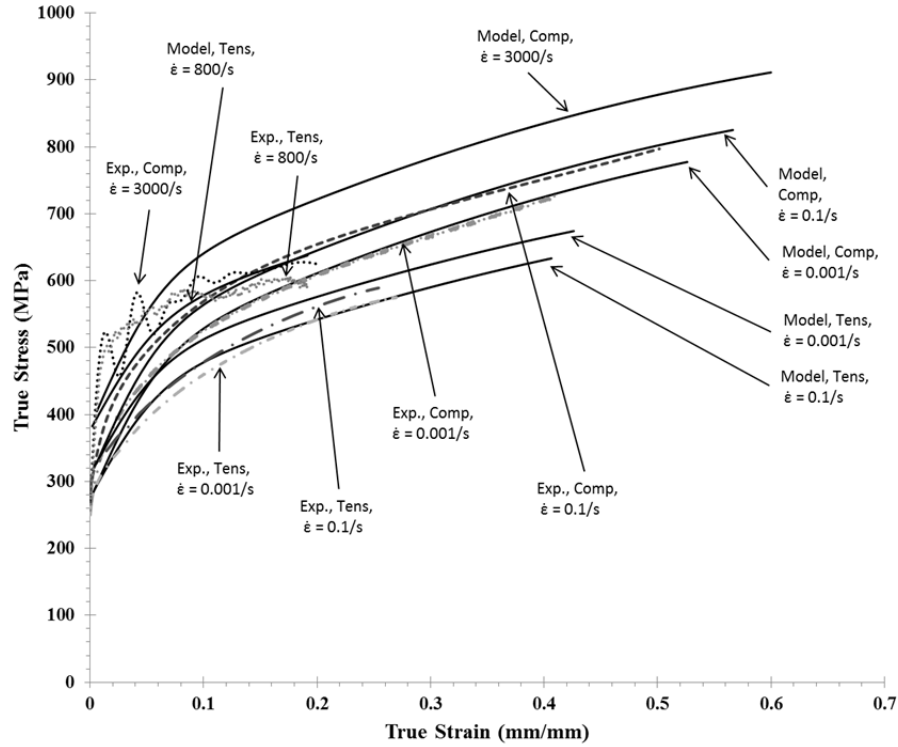


Figure 3.9 Comparison of the plasticity-damage internal state variable model with the experimental stress-strain behavior for A36 steel alloy under varying strain rates at 293K.

Now that the mechanical properties of A36 steel have been quantified we turn to the microstructural details. Samples were cut away from the plate with a water cooled saw so that any heat would not alter the microstructure shown in Figure 3.10.

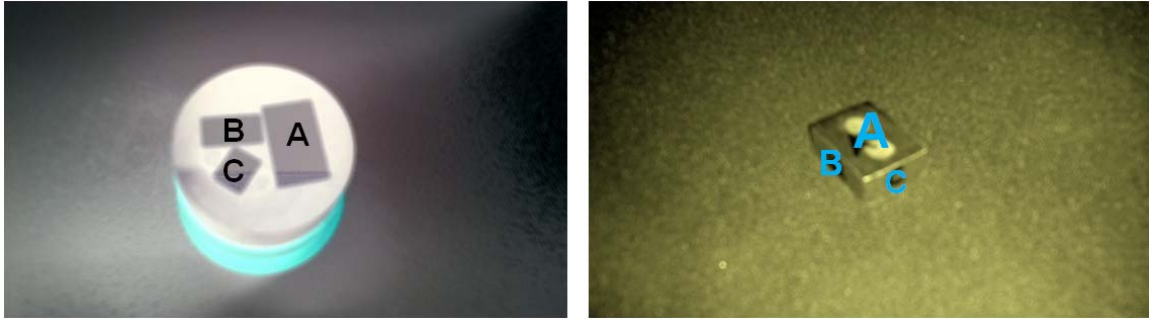


Figure 3.10 Hot mount of as-received A36 steel alloy sample showing face (A), side (B), and edge (C).

The sample was then cut to represent three different areas and hot mounted. Preparing samples in a hot mount allows for easy handling during the grinding and polishing process. After the hot mount cooled a five step process of increasing grit was performed with an automatic polisher. The final polish was performed by Vibro –polish machine for four hours. Once the sample is polished a 5% nitol solution was used to etch the sample to prepare it for viewing with an optical microscope. Etching the steel specimen rids the sample of impurities and sharpens the surface features of the sample, such as the grains. Ferrite and pearlite are the two phases found in the sample as shown in Figure 3.11 below. The darker areas are the pearlite and the lighter areas are the ferrite. No other precipitates were noticeable in the polished sample.

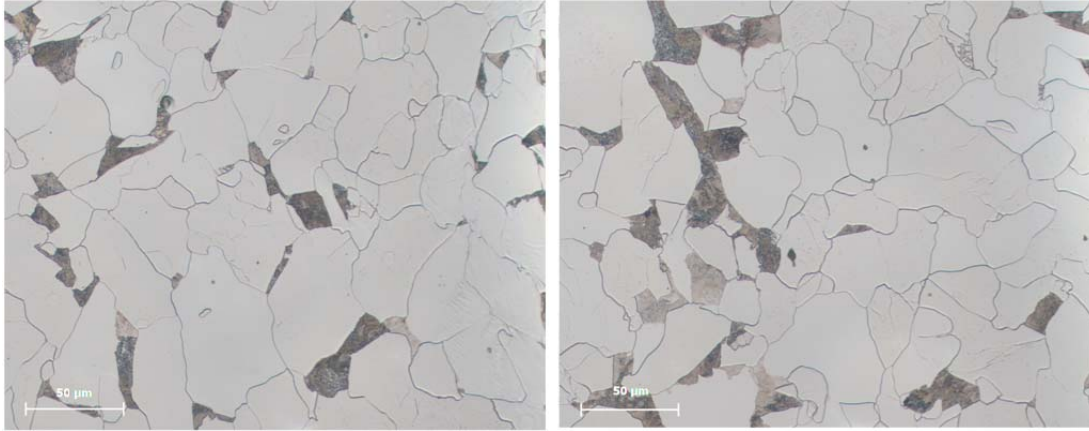


Figure 3.11 Grains structure of A36 steel alloy from optical microscope; the light area is ferrite and dark areas are pearlite.

The optical microscope was also used to perform an electronic grain analysis. The grain analysis determined the grain size was per the ASTM standard E 1382 and assigned a number of 8.50 as a mean grain size. The E1382 standard provided other information associated with this grain size number such as an average grain diameter of 16.8 μm as shown in Table 3.2. Grain volume fraction is 78.2% 7.3 ferrite and 21.8% 7.3 pearlite.

Table 3.2 Characteristics of A36 steel

Sources	σ_y (MPa)	σ_{ULT} (MPa)	$\epsilon_{Failure}$ (mm/mm)	Avg. Grain Dia. (μm)	Particle size (μ)	Particle NND (μm)	Particle VF %
A36 Plate 1.5 in. (as received)	280	650	0.23	16.8	1.78 ± 0.5	80.45 ± 64.95	0.03
ASTM standard A 36/A 36M - 05	250	400-550	0.2	N/A	N/A	N/A	N/A
Murty et al 1998	290	460	0.42	N/A	N/A	N/A	N/A
Seidt et al 2007	275	660	0.68	N/A	N/A	N/A	N/A

Information marked N/A was not reported by the source

Tension fracture samples were prepared after the mechanical testing to quantify the nucleation of A36 steel for damage model constants. Figures 3.12, 3.13, and 3.14 show the tensile fracture surfaces at the different strain rates tested.

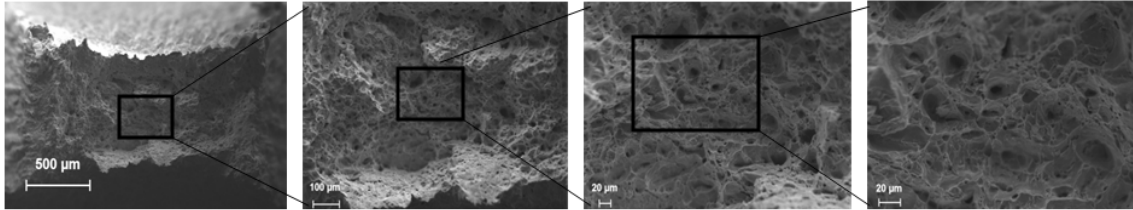


Figure 3.12 Tensile fracture surface from an applied strain rate of 0.001/s at 273 K.

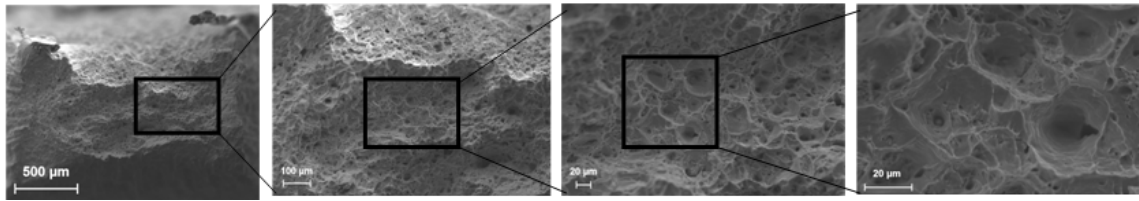


Figure 3.13 Tensile fracture surface at a strain rate of 0.1/s at 273 K.

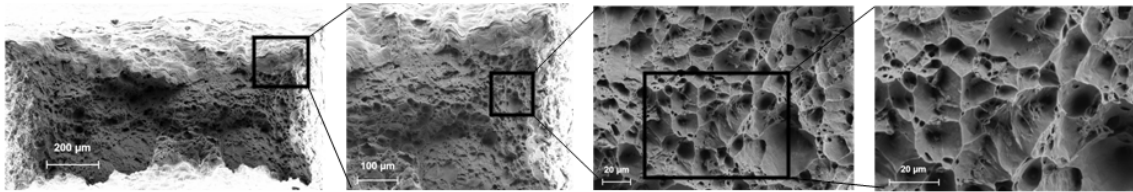


Figure 3.14 Tensile fracture surface at a strain rate of 1000/s at 273 K.

The η constant for nucleation was determined by counting the number of voids per unit area shown in Table 3.3. The highest void count occurred in the 573K tests to the dynamic strain hardening effects. Up to this point, the damage nucleation had not ever been studied on a dynamically strain aging material.

Table 3.3 The number density of voids observed on the fracture specimens.

	Quasi-static 293K	High-rate 293K	Quasi-static 573K
η	4070 mm ²	12680 mm ²	143399 mm ²
Mean void dia.	4.1 μ m	3.8 μ m	3.9 μ m
NND	5.6 μ m	3.8 μ m	4.06 μ m

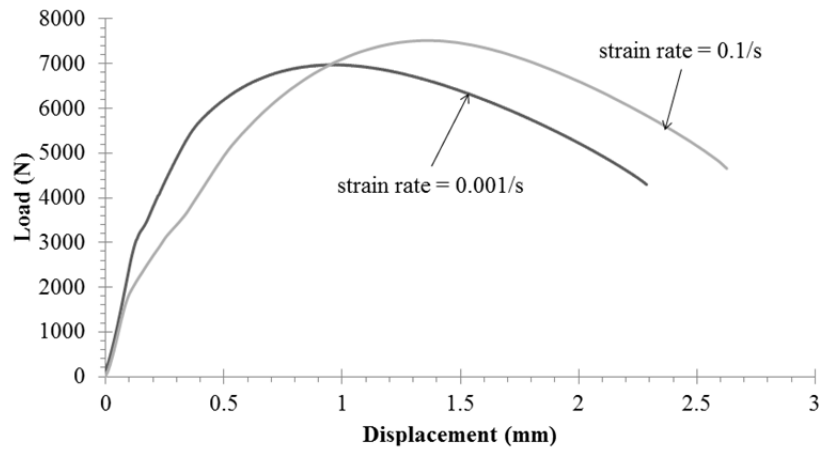


Figure 3.15 Load-displacement curve of notch A36 steel alloy specimens at two different applied strain rates (0.001/s and 0.1/s).

CHAPTER IV

A36 STEEL ALLOY I-BEAM

A Mississippi company requested help to analyze cracks in an I-Beam used in their plant for lifting bundles of tubing. The I-beam is part of an overhead hoisting system that is rated at 8000 lbs lifting capacity. After a plant worker noticed the cracks, the management wanted to determine the cause in order to decide if other I-beams used in the plant needed to be replaced. Improper use of the I-beam by overloading to twice the rated capacity developed low cycle fatigue. Failure analysis of A36 steel I-beam showed that the failure arose from fatigue initiated by a casting pore. The resulting decision was made that all I-beams were replaced in the plant. To start the I-beam analysis a sample of the I-beam was cut away and a spectrometer was used to determine the chemical composition. The I-beam is A36 steel. Table 4.1 shows the results of the spectrometer.

Table 4.1 I-Beam composition chemical composition by weight %

Element Wt. %					I-Beam
C	Mn	P	S	Si	Cu
0.52	0.98	0.009	0.018	0.259	0.08

The beam was cut down into manageable sections and delivered to CAVS as shown in Figure 4.1. The I-beam sections needed to be separated at the crack in order to analyze the crack surfaces.

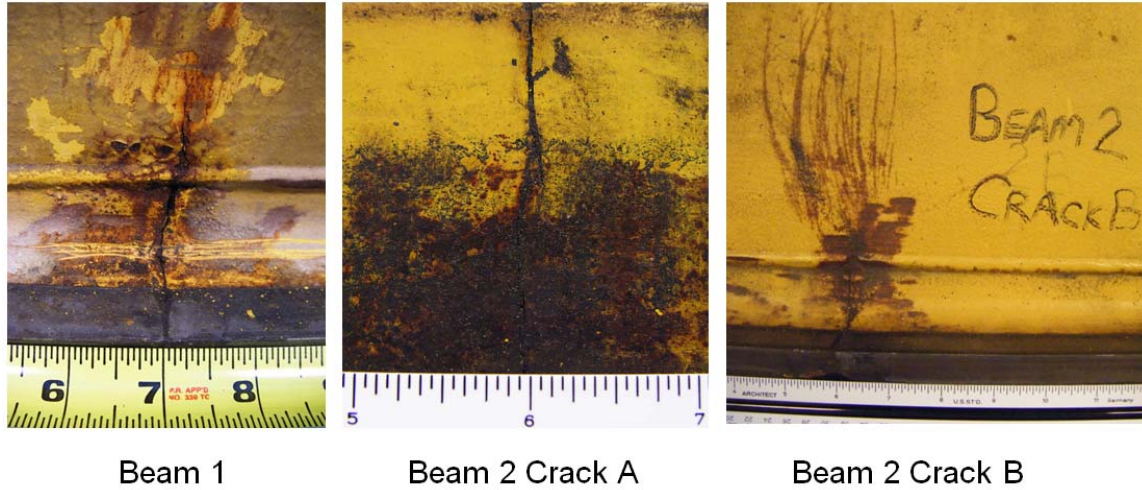


Figure 4.1 Cracks from A36 steel I-beams.

The I-beam cracks were separated using an Instron 8850 shown in figure 4.2.

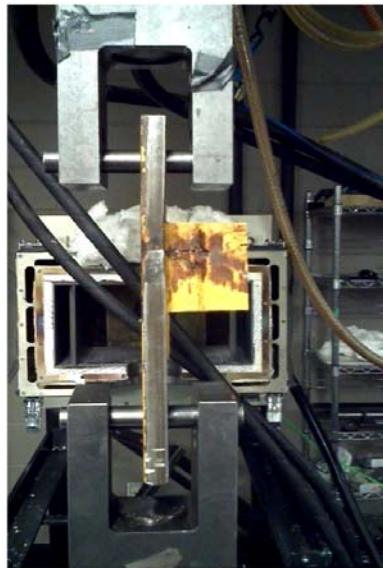


Figure 4.2 Instron 8850 and I-beam section

After the crack was carefully separated, the remaining material was reduced further to a size that would fit into a scanning electron microscope shown in Figure 4.3.

Figure 4.3 shows that the fatigue was definitely the culprit for failure as evidenced by the

striations, which designate the fatigue crack increments, and the beachmarks, which designate the different loading environments that the I-beam experienced. The striations from the different beachmarks were quantified and are shown in Figure 4.4. Figure 4.4 shows the fatigue crack growth rates (da/dN) for the different fatigue cracks within the different beachmarks. The different rates of growth indicate that several initiation points arose. After the first crack grew from a casting pore (the I-beam was made from rolled plates and welded but before the rolling procedure, the material was cast; since the sections are so thick, some remnants from the casting process, like pores, were not removed during the rolling or annealing stages), other defects near the already existing cracks initiated new fatigue cracks.

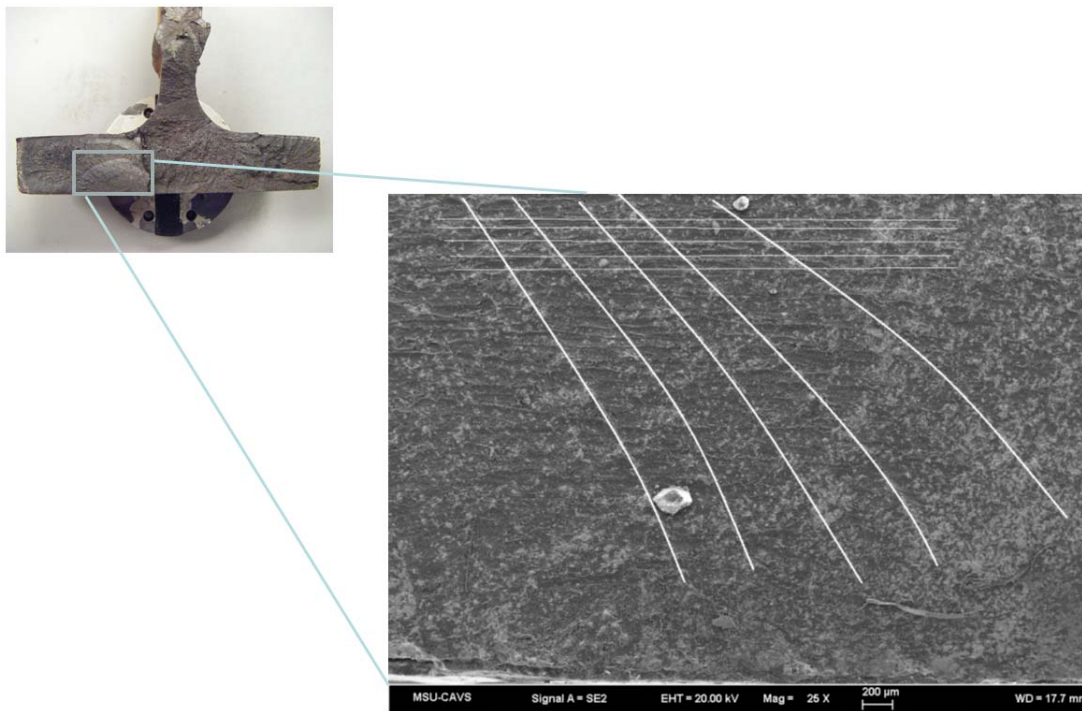


Figure 4.3 Final reduced crack section used for analysis, and the image of beachmarks and striations

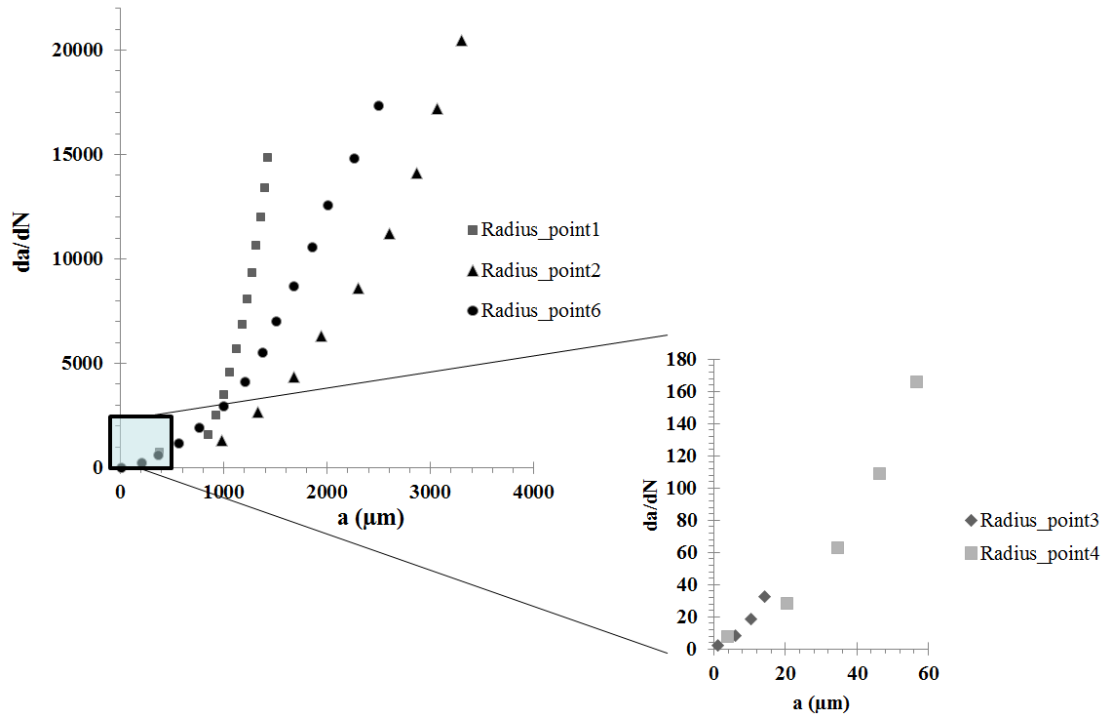


Figure 4.4 Striation measurements and crack growth rate

In order to compare the I-beam steel alloy with the A36 steel plate mechanical behavior discussed in Chapter 3, specimens were extracted from the I-beam for compression testing. Figure 4.5 shows the stress-strain behavior of the I-beam material compared to the A36 steel alloy plate discussed earlier. At two different applied strain rates (0.1/s and 0.001/s), the I-beam stress-strain behavior was clearly within the tolerance bands of the A36 steel alloy stress-strain behavior shown earlier. As such, it can be concluded that the I-beam was truly the A36 steel alloy.

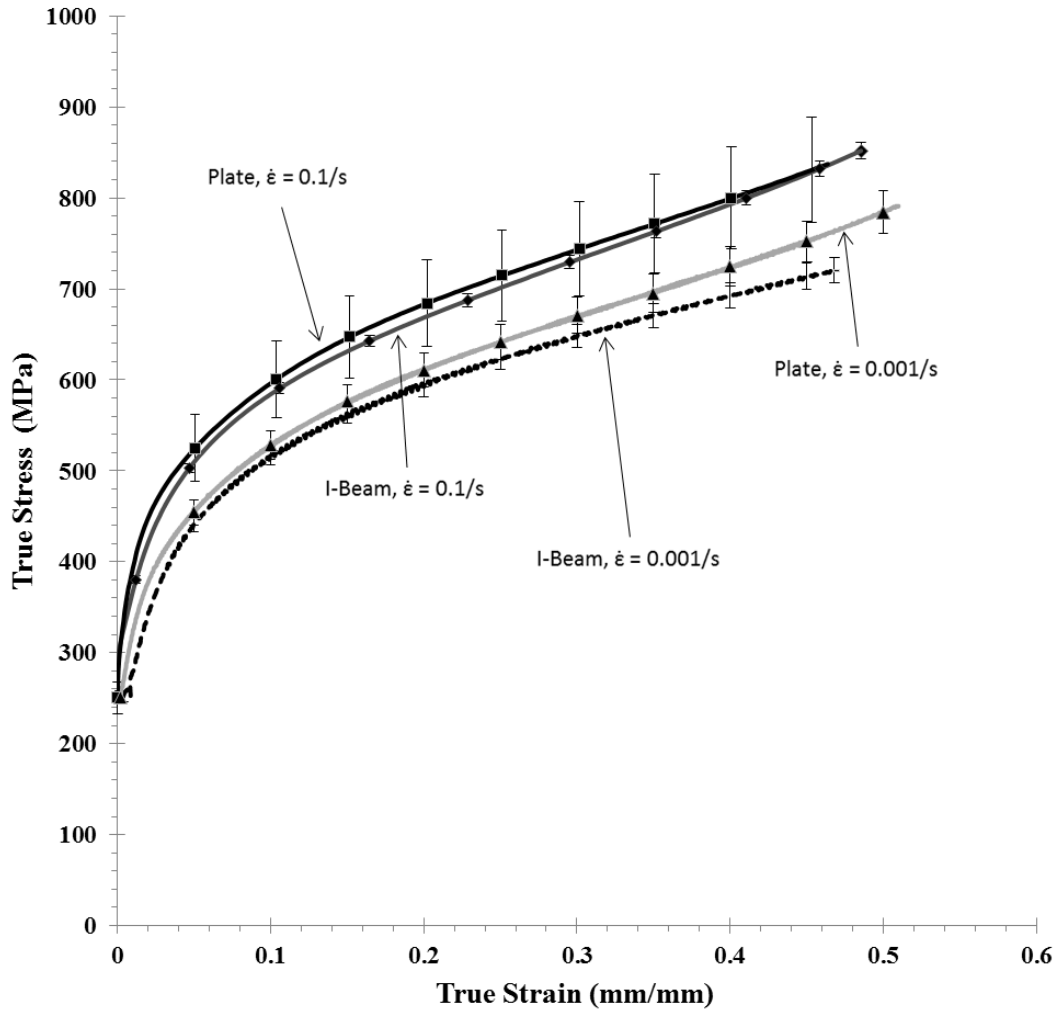


Figure 4.5 Ambient compression test comparing A36 plate steel and I-beam

CHAPTER V

CONCLUSION

- Quantified the structure-property relationships for A36 Steel for monotonic (tension and compression) fracture and fatigue loading conditions
- Calibrated the ISV plasticity-damage model for A36 steel showing the stress asymmetry between tension and compression and temperature dependence
- A manufacturing plant's A36 steel alloy I-beam failed by fatigue that initially arose because of an overload that induced a crack at a pre-existing casting pore.

REFERENCES

- ASM International, Metals Handbook*, vol. 2. 2002.
- Bammann, D. J., Chiesa, M. L., Horstemeyer, M. F., Weingarten, L. I., "Failure in Ductile Materials Using Finite Element Methods," *Structural Crashworthiness and Failure*, eds. T. Wierzbicki and N. Jones, Elsevier Applied Science, The Universities Press (Belfast) Ltd, 1993.
- Deiter, G.E., "Mechanical Metallurgy," McGraw Hill, Third edition, pp.197-205, 1986.
- Hopkinson, B., "A Method of Measuring the Pressure Produced in the Detonation of High Explosives or by the Impact of Bullets," Royal Society, pp. 437-457, 1914.
- Horstemeyer, M.F., J. Lathrop, A.M. Gokhale, M. Dighe, " Modeling stress state dependent evolution in a cast Al-Si-Mg aluminum alloy," Theoretical and applied fracture mechanics, Vol. 33, pp. 31-47, 2000.
- Johnson, G.R., W.H. Cook, A constitutive model and data for metals subjected to large strains, high strain rates and high temperatures, in: Proceedings of the Seventh International Symposium on Ballistics, The Hague, The Netherlands, April 19–21 1983, pp. 541–547.
- Kolsky, H., "An Investigation of the Mechanical Properties of Materials at very High Rates of Loading," Proc. Phys. Soc. B., 62 (11), pp. 676-700, 1949.
- Murty, K.L., M. D. Mathew, Y. Wang, V. N. Shan, and F. M. Haggag, "Nondestructive determination of tensile properties and fracture toughness of cold worked A36 steel," *International Journal of Pressure Vessels and Piping*, vol. 75, pp. 831–840, Aug. 1998.
- Roberts, R., G. V. Krishna, and J. Nishanian, "Fracture behavior of A36 bridge steels.," in *Fracture Mechanics: Twelfth Conference, ASTM STP 700*, 1980, pp. 552–577.
- Seidt, J.D., A. Gilat, and J. A. Klein, "High strain rate, high temperature constitutive and failure models for EOD impact scenerios," in *Proceedings of the SEM Annual Conference and Exposition on Experimental and Applied Mechanics*, 2007, vol. 1, pp. 160–174.
- Wang, H.D., Berdin, C., Maziere, M., Forest, S., Prioul, C., Parrot, A., and Le-Delliou, "Experimental and numerical study of dynamic strain ageing and its relation to ductile fracture of a C–Mn steel," *Matl. Sci. Eng. A.*, Vol. 547, No. 15, pp. 19-31, 2012.

APPENDIX A

MICROSTRUCTURE-PROPERTY MODEL EQUATIONS (MACROSCALE)

Stress – strain relationships

$$\dot{\underline{\sigma}} = \dot{\underline{\sigma}} - \underline{W}^e \underline{\sigma} - \underline{\sigma} \underline{W}^e = \lambda(1-D) \text{tr}(\underline{D}^e) \underline{I} + 2\mu(1-D) \underline{D}^e - \frac{\dot{D}}{1-D} \underline{\sigma} \quad \text{Eq. A1}$$

$$\underline{D}^e = \underline{D} - \underline{D}^{in} \quad \text{Eq. A2}$$

$$\underline{D}^{in} = f(T) \sinh \left[\frac{\|\underline{\sigma}' - \underline{\alpha}\| - \{R + Y(T)\}\{1-D\}}{V(T)\{1-D\}} \right] \frac{\underline{\sigma}' - \underline{\alpha}}{\|\underline{\sigma}' - \underline{\alpha}\|} \quad \text{Eq. A3}$$

Dislocation - Plasticity internal state variables

$$\dot{\underline{\alpha}} = \dot{\underline{\alpha}} - \underline{W}^e \underline{\alpha} + \underline{\alpha} \underline{W}^e = \left\{ h(T) \underline{D}^{in} - \left[\sqrt{\frac{2}{3}} r_d(T) \|\underline{D}^{in}\| + r_s(T) \right] \|\underline{\alpha}\| \underline{\alpha} \right\} \left[\frac{DCS_0}{DCS} \right]^z \quad \text{Eq. A4}$$

$$\dot{R} = \left\{ H(T) \underline{D}^{in} - \left[\sqrt{\frac{2}{3}} R_d(T) \|\underline{D}^{in}\| + R_s(T) \right] R^2 \right\} \left[\frac{DCS_0}{DCS} \right]^z \quad \text{Eq. A5}$$

Damage internal state variables

$$\dot{D} = [\dot{\phi}_{particles} + \dot{\phi}_{pores}] c + [\phi_{particles} + \phi_{pores}] \dot{c} \quad \text{Eq. A6}$$

$$\dot{\eta} = \|\underline{D}^{in}\| \frac{d^{1/2}}{K_{IC} f^{1/2}} \eta \left\{ a \left[\frac{4}{27} - \frac{J_3^2}{J_2^3} \right] + b \frac{J_3}{J_2^{3/2}} + c \left\| \frac{I_1}{\sqrt{J_2}} \right\| \right\} \exp \left(- \frac{C_{\eta T}}{T} \right) \quad \text{Eq. A7}$$

$$\dot{\phi}_{particles} = \dot{\eta} v + \eta \dot{v} \quad \text{Eq. A8}$$

$$\dot{v} = \frac{3}{2} v \left[\frac{3}{2} \frac{V(T)}{Y(T)} \frac{\sigma_H}{\sigma_{vm}} + \left(1 - \frac{V(T)}{Y(T)} \right) (1 + 0.4319) \right]^{Y(T)/V(T)} \underline{D}^{in} \quad \text{Eq. A9}$$

$$\dot{\phi}_{pores} = \left[\frac{1}{(1 - \phi_{pores})^m} - (1 - \phi_{pores}) \right] \sinh \left\{ \frac{2 \left(2^{V(T)/Y(T)} - 1 \right) \sigma_H}{\left(2^{V(T)/Y(T)} + 1 \right) \sigma_{17M}} \right\} \|D^{in}\|$$

Eq. A10

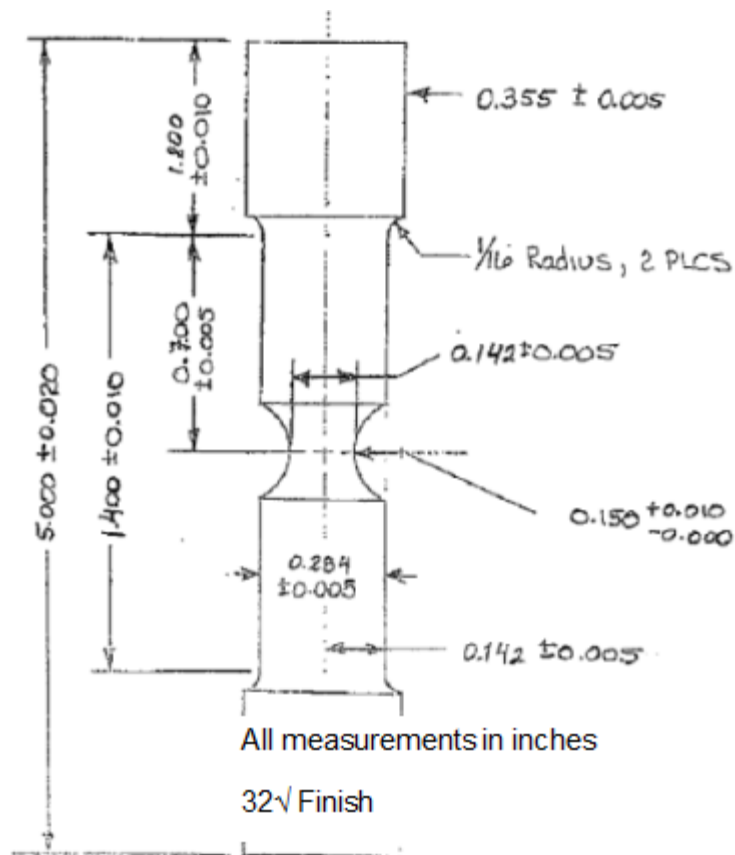
$$\dot{c} = C_{coef} [\eta \dot{\nu} + i \eta \nu] \exp(C_{CT} T) \left(\frac{DCS_0}{DCS} \right)^z$$

Eq. A11

C1= 7.55	Ca= 0
C2= 0	Cb= -0.3
C3= 140	an= 0
C4= 133	bn= 0
C5= 1e-006	cn= 0
C6= 0	Ccoef= 0
C7= 0.0944	cd1= 0
C8= 0	cd2= 0
C9= 2816	Z= 0
C10= 0	C21= 0
C11= 0	C22= 0
C12= 0	C23= 0
C13= 0.004	C24= 0
C14= 0	C25= 0
C15= 703	C26= 0
C16= 0	NTD= 0
C17= 0	CTD= 0
C18= 0	CAcon= 0.5
C19= 0	
C20= 0	

Figure A.1 Constants for MSU Internal State Variable Plasticity-Damage Model

APPENDIX B
MECHANICAL SPECIMENS



$$2a = 0.142 \text{ in.}$$

$$r = 0.150 \text{ in.}$$

$$\frac{a}{r} = \frac{0.071}{0.150} = 0.47$$

Figure B.1 Mechanical test notch specimen.


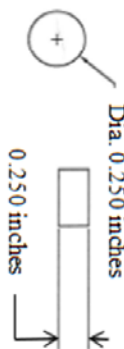
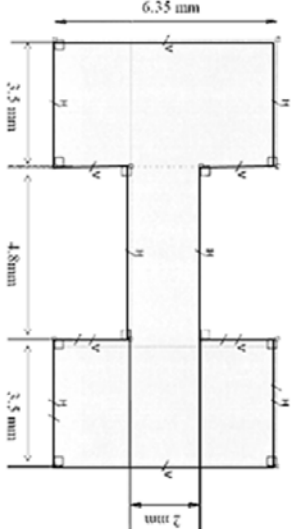
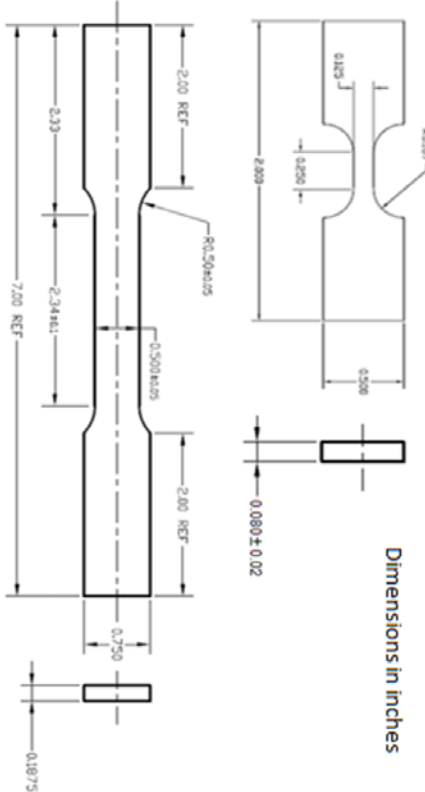
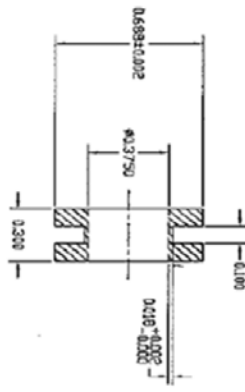
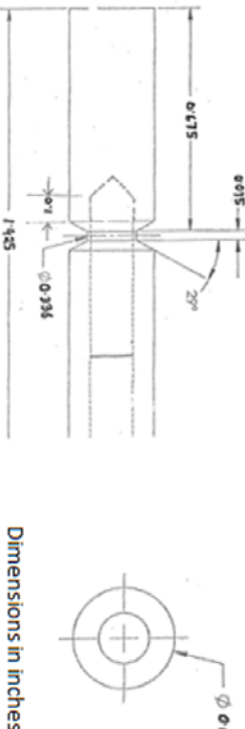
Test type	Hopkinson Bar / High rate	Quasi - static
Compression	 <p>Dia. 0.250 inches 0.250 inches</p>	 <p>Dia. 0.250 inches 0.250 inches</p>
Tensile	 <p>Dimensions in metric</p>	 <p>Dimensions in inches</p>
Torsion	 <p>Dimensions in inches</p>	 <p>Dimensions in inches</p>

Figure B.2 Mechanical test specimens